



Research Article

TiO₂/g-C₃N₄ Visible-Light-Driven Photocatalyst for Methylene Blue Decomposition

Dang Thi Ngoc Hoa,^{1,2} Nguyen Thi Thanh Tu ,³ Huynh Quoc An Thinh,² Le Van Thanh Son,⁴ Le Vu Truong Son,⁴ Nguyen Duc Vu Quyen,² Le Lam Son,² Tran Ngoc Tuyen,² Pham Le Minh Thong,⁵ Ly Hoang Diem,⁶ and Dinh Quang Khieu ²

¹University of Medicine and Pharmacy, Hue University, Hue 530000, Vietnam

²University of Sciences, Hue University, Hue 530000, Vietnam

³Faculty of Applied Technology, School of Technology, Van Lang University, Ho Chi Minh City 700000, Vietnam

⁴University of Education and Science, The University of Danang, Da Nang 550000, Vietnam

⁵Institute of Research and Development, Duy Tan University, Da Nang 550000, Vietnam

⁶Kien Giang University, Kien Giang 920000, Vietnam

Correspondence should be addressed to Nguyen Thi Thanh Tu; tu.ntt@vlu.edu.vn and Dinh Quang Khieu; dqkhieu@hueuni.edu.vn

Received 7 June 2022; Revised 5 October 2022; Accepted 13 October 2022; Published 1 February 2023

Academic Editor: Ganesan Sriram

Copyright © 2023 Dang Thi Ngoc Hoa et al. This is an open access article distributed under the Creative Commons Attribution License, which permits unrestricted use, distribution, and reproduction in any medium, provided the original work is properly cited.

In this work, graphitic carbon nitride (*g*-C₃N₄)/titanium dioxide (TiO₂) nanoparticles with heterostructures were synthesized *in situ* from a mixture of melamine and peroxo-titanium complexes in a calcination process. The TiO₂ nanoparticles are well-dispersed on the *g*-C₃N₄ nanosheets. The prepared TiO₂/*g*-C₃N₄ composites have a heterostructure and excellent photocatalytic activity for decomposing methylene blue (MB) under visible light irradiation. The as-obtained *g*-C₃N₄ embroiled with TiO₂ has a much larger surface area than its components (66.7 and 6.6 m²·g⁻¹ for TiO₂ and *g*-C₃N₄ against 95.5–143.8 m²·g⁻¹ for the composite, respectively). It enhances the separation of photo-generated charge carriers. The TiO₂/*g*-C₃N₄ photocatalytic degradation of MB was investigated in aqueous heterogeneous suspensions. The experimental kinetic data for the photocatalytic process follow the pseudo-first-order kinetic model. Furthermore, TiO₂/*g*-C₃N₄ retains high photocatalytic activity after four reaction cycles. In addition to prompt removal of the color, the TiO₂/*g*-C₃N₄ photocatalyst can oxidize MB almost completely to final oxidation products. The pathway of MB decomposition was also addressed. Additionally, the TiO₂/*g*-C₃N₄ photocatalytic system was employed to eliminate other typical organic pigments, such as malachite green, methyl blue, and methyl red. The TiO₂/*g*-C₃N₄ material, with remarkable dye degradability, is a promising catalyst in industrial textile treatment and can find applications in light-harvesting systems.

1. Introduction

Recently, graphitic carbon nitride (*g*-C₃N₄) has become prominent as a stable photocatalyst and gained significant attention [1] owing to its relevant bandgap (2.7 eV) [2] and, therefore, can be active under visible light. In addition, the negative potential (−1.12 eV vs. normal hydrogen electrode (NHE)) of the conduction band (CB) enables *g*-C₃N₄ to form heterojunctions with other semiconductors. Despite its disadvantages, such as small surface area and high recombination

rate of photoinduced charge carriers, *g*-C₃N₄ is still a potential candidate for hybrid heterostructures with wide bandgap semiconductors [3].

Besides various semiconducting materials, such as SnO₂, ZnO, ZnS, WO₃, and V₂O₅ [4], TiO₂ has attracted tremendous attention in photocatalytic applications because of its low cost, high stability, nontoxic nature, and environmental friendliness. Although TiO₂ has been used in several photocatalytic processes of wastewater treatment and air purification [5], its wide bandgap (3.2 eV) [6] limits its application

only to the ultraviolet region of visible light, which is around only 4% of the solar spectrum. To overcome this disadvantage, doping other nonmetallic or trace metallic elements, such as N, P, Fe, Ni, and V, to develop composite materials with narrow-band energy has been studied intensively [4, 7, 8]. Numerous studies have presented the feasibility of synthesizing $\text{TiO}_2/g\text{-C}_3\text{N}_4$ photocatalysts [9]. Using $g\text{-C}_3\text{N}_4$ with TiO_2 to form a heterojunction is one of the efficient approaches for either narrowing bandgap or enhancing photoinduced electron–hole pair separation. For example, Liu et al. [10] synthesized $\text{TiO}_2/g\text{-C}_3\text{N}_4$ from TiO_2 and urea and utilized this material to promote the photocatalytic reduction of U(VI) in water. Zhang et al. [11] and Alcudia-Ramos et al. [12] fabricated $\text{TiO}_2/g\text{-C}_3\text{N}_4$ from tetrabutyl titanate or TiOSO_4 and urea to enhance photocatalytic hydrogen evolution under visible light. Titanium alkoxides, TiCl_3 , and TiCl_4 in a hydrochloric acid aqueous solution or $\text{Ti}(\text{SO}_4)_2$ in a sulfuric acid aqueous solution are mainly used as a titanium source [11, 12]. However, titanium alkoxides, such as tetra-isopropoxide, are highly unstable, flammable, and readily hydrolyze in a moist atmosphere. Moreover, titanium chlorides in these acidic solutions are difficult to handle because of their aggressive and toxic nature. For solving these issues, insensitive approaches have been investigated in developing water-soluble titanium complexes, such as peroxo-titanium oxalate and peroxo-titanium complexes [13], for synthesizing titanium-dioxide-based materials [14]. To our best knowledge, reports on the TiO_2 -based materials synthesized via water-soluble titanium species are limited. Therefore, we developed a strategy for preparing $\text{TiO}_2/g\text{-C}_3\text{N}_4$ from a water-soluble titanium complex and melamine solution to form a homogeneous mixture in this study. The peroxo–hydro titanium complexes were synthesized from titanium oxide in a hydrothermal process, followed by the formation of water-soluble titanium complexes with hydrogen peroxide. $\text{TiO}_2/g\text{-C}_3\text{N}_4$ was then prepared by evaporating the homogeneous complex solution, followed by calcination. The photocatalytic activity of $\text{TiO}_2/g\text{-C}_3\text{N}_4$ was studied via the kinetics, mineralization, photocatalytic mechanism, and decomposition pathway of methylene blue.

2. Experimental

2.1. Materials. Anatase (TiO_2 , 99%) and melamine ($\text{C}_3\text{H}_6\text{N}_6$, $\geq 99.5\%$) were purchased from Merck. Potassium iodide (KI, $\geq 99\%$), sodium chloride (NaCl , $\geq 99.5\%$), sodium hydroxide (NaOH , $\geq 96\%$), hydrochloric acid (HCl , 38%), hydrogen peroxide (H_2O_2 , $\geq 30\%$), and isopropanol ($\text{CH}_3\text{CH}(\text{OH})\text{CH}_3$, $\geq 99.8\%$) were obtained from Xilong, China. Methylene blue ($\text{C}_{16}\text{H}_{18}\text{N}_3\text{SCl}\cdot 3\text{H}_2\text{O}$, MB), methyl red ($\text{C}_{15}\text{H}_{15}\text{N}_3\text{O}_2$, MR), methyl blue ($\text{C}_{37}\text{H}_{27}\text{N}_3\text{Na}_2\text{O}_9\text{S}_3$, MyB), malachite green ($\text{C}_{28}\text{H}_{30}\text{N}_2\text{O}_3$, $\geq 96.5\%$, MG), and *p*-benzoquinone ($\text{C}_6\text{H}_4\text{O}_2$, $\geq 99\%$) were provided by Sigma–Aldrich. All the chemicals were of analytical grade and used as received without any further purification.

2.2. Synthesis of $g\text{-C}_3\text{N}_4$. According to Yan et al. [1], the $g\text{-C}_3\text{N}_4$ material was synthesized from melamine. Briefly, 10 g of melamine powder was weighed, placed in a mortar, and finely ground. The powder was put into a porcelain

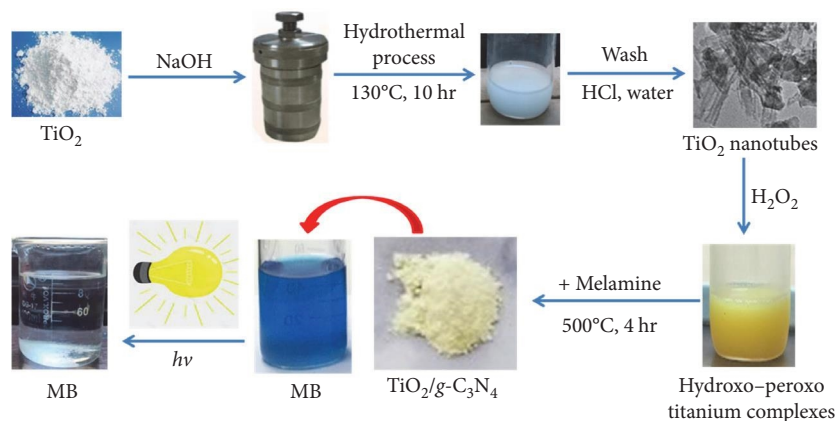
cup and calcined at 500°C for 4 hr with a heating rate of $5^\circ/\text{min}$. The powder was cooled to ambient temperature and finely grounded to obtain a yellow product, denoted as $g\text{-C}_3\text{N}_4$.

2.3. Synthesis of Peroxo-Titanium Complexes. According to Chau et al. [15] and Le et al. [16], the peroxo–hydroxo titanium(IV) complex was synthesized. Briefly, 0.25 g of TiO_2 powder was dispersed into 12.5 mL of a 20 M NaOH solution under sonication for about 15 min. Then, the entire solution was transferred to a Teflon flask and heated at 130°C for 10 hr. After cooling to ambient temperature, the white solid was separated and rinsed with distilled water and a 0.1 M HCl solution to completely remove the alkali then dried at 80°C for 2 hr (around 0.189 g of dried TiO_2 obtained). The 4.62 mg of hydrothermal-treated TiO_2 was added 35 mL of 30% H_2O_2 at 90°C , stirring for 1 hr to obtain a clear yellow solution (the solution is stable at 10°C for several days). The obtained peroxo-titanium complexes solution has a composition of 4.62 mg $\text{TiO}_2/35$ mL determined with the gravity method.

2.4. Synthesis of $\text{TiO}_2/g\text{-C}_3\text{N}_4$. $\text{TiO}_2/g\text{-C}_3\text{N}_4$ composites were synthesized via an aqueous solution process: a mixture of titanium peroxo-titanium complex solution (35 mL; 4.62 mg TiO_2) and (0.00; 1.16; 4.62; 18.48 mg) with known $\text{TiO}_2/\text{melamine}$ mass ratios was sonicated for 1 hr, followed by calcination at 500°C for 4 hr to obtain a $\text{TiO}_2/g\text{-C}_3\text{N}_4$ composite. The mixtures are denoted as (10/0) $\text{TiO}_2/g\text{-C}_3\text{N}_4$, (8/2) $\text{TiO}_2/g\text{-C}_3\text{N}_4$, (5/5) $\text{TiO}_2/g\text{-C}_3\text{N}_4$, (2/8) $\text{TiO}_2/g\text{-C}_3\text{N}_4$, and (0/10) $\text{TiO}_2/g\text{-C}_3\text{N}_4$, where the fraction in the parentheses is the $\text{TiO}_2/\text{melamine}$ mass ratio. The synthetic diagram is shown in Scheme 1.

2.5. Material Characterization. X-ray diffraction (XRD) was performed on a D8 Advance device (Bruker, USA) with a $\text{Cu}/K\alpha$ radiation source and $\lambda = 0.154056$ nm. Scanning electron microscopy (SEM) images were collected by using an SEM Hitachi-S-4800, Japan, scanning electron microscope. FT infrared (FTIR) spectra for the samples were obtained on an IRAffinity-1S-Shimadzu spectrometer (Japan). Specific surface areas were determined from N_2 adsorption–desorption isotherms in liquid nitrogen at 77 K by using a Micromeritics ASAP 2020 analyzer. UV–vis DR spectra were obtained on a UV2600-Shimadzu spectrometer (Japan).

2.6. Catalytic Activity. The catalytic activity of the obtained materials was studied via the decomposition of methylene blue (10 ppm) on the catalyst (0.2 g/L). The mixture was stirred in the dark for 40 min to reach the adsorption/desorption equilibrium, then illuminated with an Osram, 160 W filament lamp (filter cutoff $\lambda < 420$ nm). The MB concentration in the supernatant was determined by using UV–vis spectroscopy at a maximum wavelength of 664 nm. The pH value of the dye solutions was adjusted with 0.1 M HCl or 0.1 M NaOH solutions. In addition, the concentration of malachite green was determined at 617 nm and methyl red at 521 nm. The UV–vis spectra were recorded on a Spectro UV-2650 spectrometer (Labomed, Inc., USA). The chemical oxygen demand (COD) was determined by using a Thermoreactor Lovibond ET108 analyzer according to the dichromate



SCHEME 1: The diagram for the preparation of $\text{TiO}_2/\text{g-C}_3\text{N}_4$ composites.

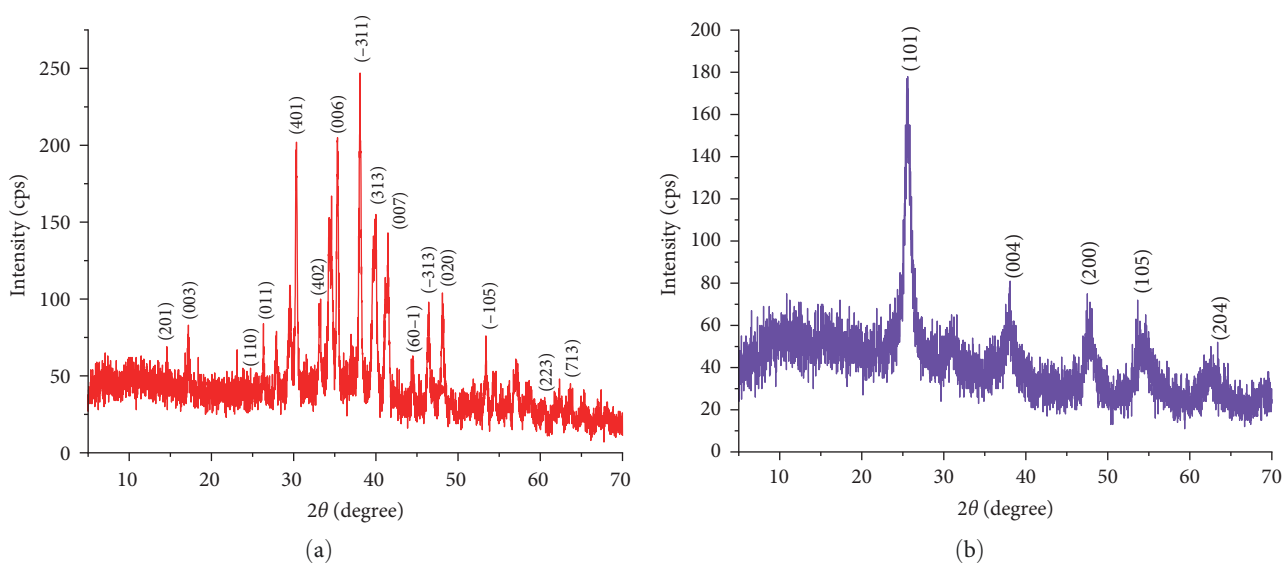


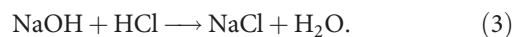
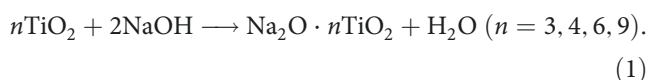
FIGURE 1: (a) XRD patterns of sodium titanate; (b) TiO_2 after alkaline removal.

method. The intermediates that appear during MB degradation were extracted and accumulated by chloroform, then determined by the ion trap method in combination with EIS ionized mass spectroscopy on a LC/MSD Trap-SL ion trap mass spectrometer. ICP analysis for titanium was performed using a 7800 ICP-MS instrument (Agilent Technologies, Santa Clara, CA, USA).

3. Results and Discussion

Figure 1 presents the XRD patterns of the products synthesized under different conditions. Anatase (TiO_2) reacts with NaOH to create several forms of sodium titanate at 130°C and 10 hr. The characteristic peaks of $\text{Na}_2\text{Ti}_3\text{O}_7$ indexed as (011), (-311), (-313), and (-105); $\text{Na}_2\text{Ti}_6\text{O}_{13}$ indexed as (201), (110), (401), (402), (313), (223), and (713) and $\text{Na}_2\text{Ti}_9\text{O}_{19}$ indexed as (003), (006), (007), (60-1), and (020) according to JCPDS 31-1329, JCPDS 73-1398, JCPDS 33-1293, respectively, are present in the XRD patterns (Figure 1(a)). The sodium titanates after being rinsed with HCl until neutral filtrates change to anatase TiO_2 (JCPDS 21-1272) (Figure 1(b)). The

preparation of water-soluble peroxo-titanium complexes is associated with the formation of peroxo-titanium complexes, such as $[\text{Ti}(\text{O}_2)(\text{OH})]^+$, $[\text{Ti}(\text{O}_2)(\text{OH})_2]$, and $[\text{Ti}(\text{O}_2)(\text{OH})_3]^-$, which dimerize and result in various oxo-peroxo-hydroxo di-titanium complexes, such as $\text{Ti}_2(\text{O})(\text{O}_2)_2(\text{OH})_2$, $[\text{Ti}_2(\text{O})(\text{O}_2)_2(\text{OH})_3]^-$, and $[\text{Ti}_2(\text{O})(\text{O}_2)_2(\text{OH})_4]^{2-}$. These dimeric complexes can undergo further self-condensation to form oligomers. As a result, polynuclear oxo-peroxo-hydroxo titanium complexes precipitate as $[\text{Ti}_2(\text{O})(\text{O}_2)_2(\text{OH})_2]_n$ [17] (Equations (1)–(4)).



In the synthesis of the $\text{TiO}_2/\text{g-C}_3\text{N}_4$ composite, different peroxo-titanium complexes/melamine mass ratios were used.

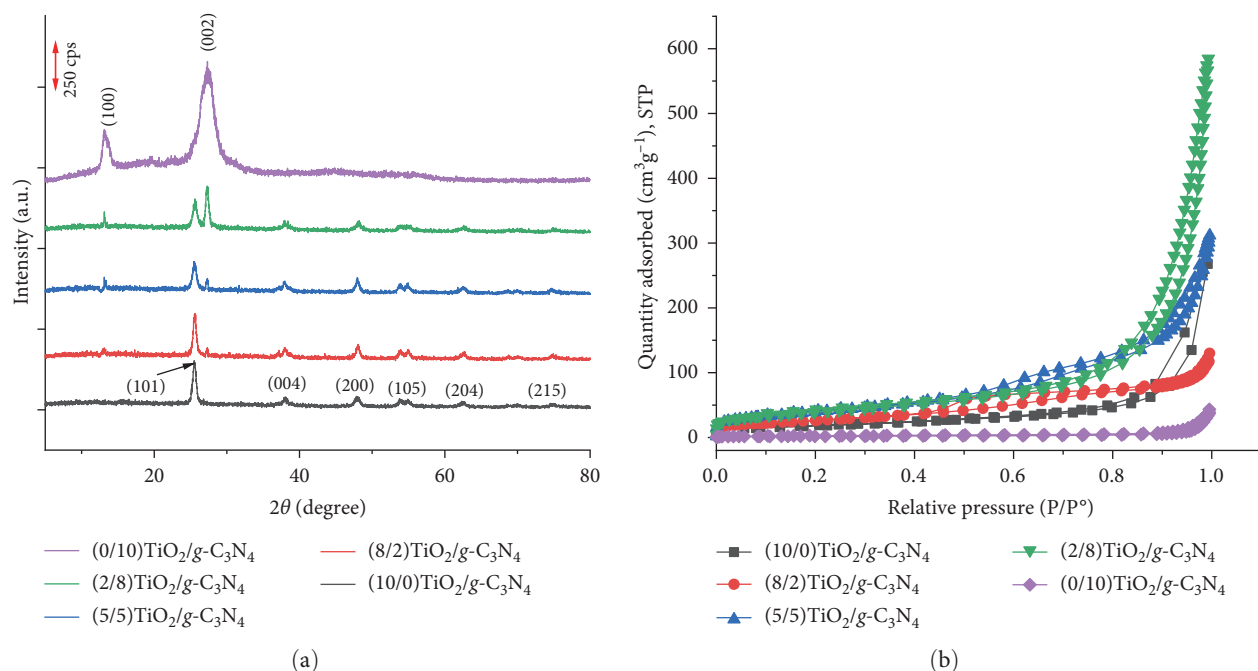


FIGURE 2: XRD patterns (a) and nitrogen adsorption/desorption isotherms, (b) of (10/0) $\text{TiO}_2/\text{g-C}_3\text{N}_4$; (8/2) $\text{TiO}_2/\text{g-C}_3\text{N}_4$; (5/5) $\text{TiO}_2/\text{g-C}_3\text{N}_4$; (2/8) $\text{TiO}_2/\text{g-C}_3\text{N}_4$; (0/10) $\text{TiO}_2/\text{g-C}_3\text{N}_4$.

TABLE 1: The textural properties of $\text{TiO}_2/\text{g-C}_3\text{N}_4$.

Notation	S_{BET} ($\text{m}^2\cdot\text{g}^{-1}$)	S_{meso} ($\text{m}^2\cdot\text{g}^{-1}$)	S_{micro} ($\text{m}^2\cdot\text{g}^{-1}$)	V_{total} ($\text{cm}^3\cdot\text{g}^{-1}$)
(10/0) $\text{TiO}_2/\text{g-C}_3\text{N}_4$	66.7	63.6	3.1	267.7
(8/2) $\text{TiO}_2/\text{g-C}_3\text{N}_4$	95.5	71.0	24.5	130.0
(5/5) $\text{TiO}_2/\text{g-C}_3\text{N}_4$	139.5	98.7	40.8	584.6
(2/8) $\text{TiO}_2/\text{g-C}_3\text{N}_4$	143.8	102.9	40.9	311.8
(0/10) $\text{TiO}_2/\text{g-C}_3\text{N}_4$	6.6	4.2	2.4	43.3

Figure 2(a) presents the XRD patterns of pristine $\text{g-C}_3\text{N}_4$, TiO_2 , and $\text{TiO}_2/\text{g-C}_3\text{N}_4$ composites. For the pristine $\text{g-C}_3\text{N}_4$ and TiO_2 , the characteristic peaks of the $\text{g-C}_3\text{N}_4$ phase are observed on the XRD pattern of (0/10) $\text{TiO}_2/\text{g-C}_3\text{N}_4$ at 13° and 27° , indexed as (100) and (002) (JCPDS 87-1526). These two peaks are likely assigned to the structure of the tri-*s*-triazine unit with interplanar spacing and the conjugated aromatic system [18]. This observation confirms the presence of $\text{g-C}_3\text{N}_4$ in the sample. The XRD pattern of (10/0) $\text{TiO}_2/\text{g-C}_3\text{N}_4$ exhibits characteristic peaks at 25.2° , 37.8° , 48.0° , 53.8° , 62.6° , 70.3° , and 75.0° corresponding to (101), (004), (200), (105), (204), (220), and (215) Miller index, respectively (JCPDS 21-1272). These peaks suggest the TiO_2 anatase form. The characteristic peaks of both TiO_2 and $\text{g-C}_3\text{N}_4$ are observed in the XRD patterns of $\text{TiO}_2/\text{g-C}_3\text{N}_4$ composites. The increasing amount of $\text{g-C}_3\text{N}_4$ augments the intensity of its characteristic peaks.

The textural properties of the obtained composites were studied via their nitrogen adsorption/desorption isotherms (Figure 2(b)). All the isotherm curves of $\text{g-C}_3\text{N}_4$, TiO_2 , and its composite belong to the IV type according to the IUPAC classification with the H3 hysteresis loop at relative pressures 0.6–1, suggesting the mesoporous structures formed from fine particles. The surface area of $\text{g-C}_3\text{N}_4$ and TiO_2 is similar

to what was reported previously [19, 20]. It is worth noting that the composites have a significantly larger surface area than $\text{g-C}_3\text{N}_4$ and TiO_2 (95.5 – $143.8 \text{ m}^2\cdot\text{g}^{-1}$ compared with 66.7 and $6.6 \text{ m}^2\cdot\text{g}^{-1}$) (Table 1).

Table 1 shows that the surface area of the composite results mainly from the mesoporous area. Both $\text{g-C}_3\text{N}_4$ and TiO_2 enhance the microporous and mesoporous spaces. The reason could be that the initial precursor of both titania and melamine in the liquid form is favorable for creating a homogeneous mixture. During heating, the gas products are generated to form the porous structure of $\text{TiO}_2/\text{g-C}_3\text{N}_4$. The (2/8) $\text{TiO}_2/\text{g-C}_3\text{N}_4$ sample exhibits the largest surface area ($143.8 \text{ m}^2\cdot\text{g}^{-1}$), higher than the $\text{TiO}_2/\text{g-C}_3\text{N}_4$ samples synthesized from titanium *n*-butoxide and urea ($62.1 \text{ m}^2\cdot\text{g}^{-1}$) [21] and TiO_2 powder and melamine ($97.26 \text{ m}^2\cdot\text{g}^{-1}$) [22].

Figure 3(a) presents the FTIR spectra of $\text{g-C}_3\text{N}_4$, TiO_2 , and $\text{TiO}_2/\text{g-C}_3\text{N}_4$ composites. For bare $\text{g-C}_3\text{N}_4$ and TiO_2 , the vibration at 810 cm^{-1} is related to the C–N ring of the tri-*s*-triazine unit. The peaks at $1,238$, $1,316$, and $1,402 \text{ cm}^{-1}$ are attributed to the stretching vibrations of the C–NH bond in $\text{g-C}_3\text{N}_4$. The peaks at $1,637$ and $3,000$ – $3,500 \text{ cm}^{-1}$ are assigned to the stretching vibration of C=N [21, 23] and –N–H or =N–H bond [23, 24]. The stretching vibrations of

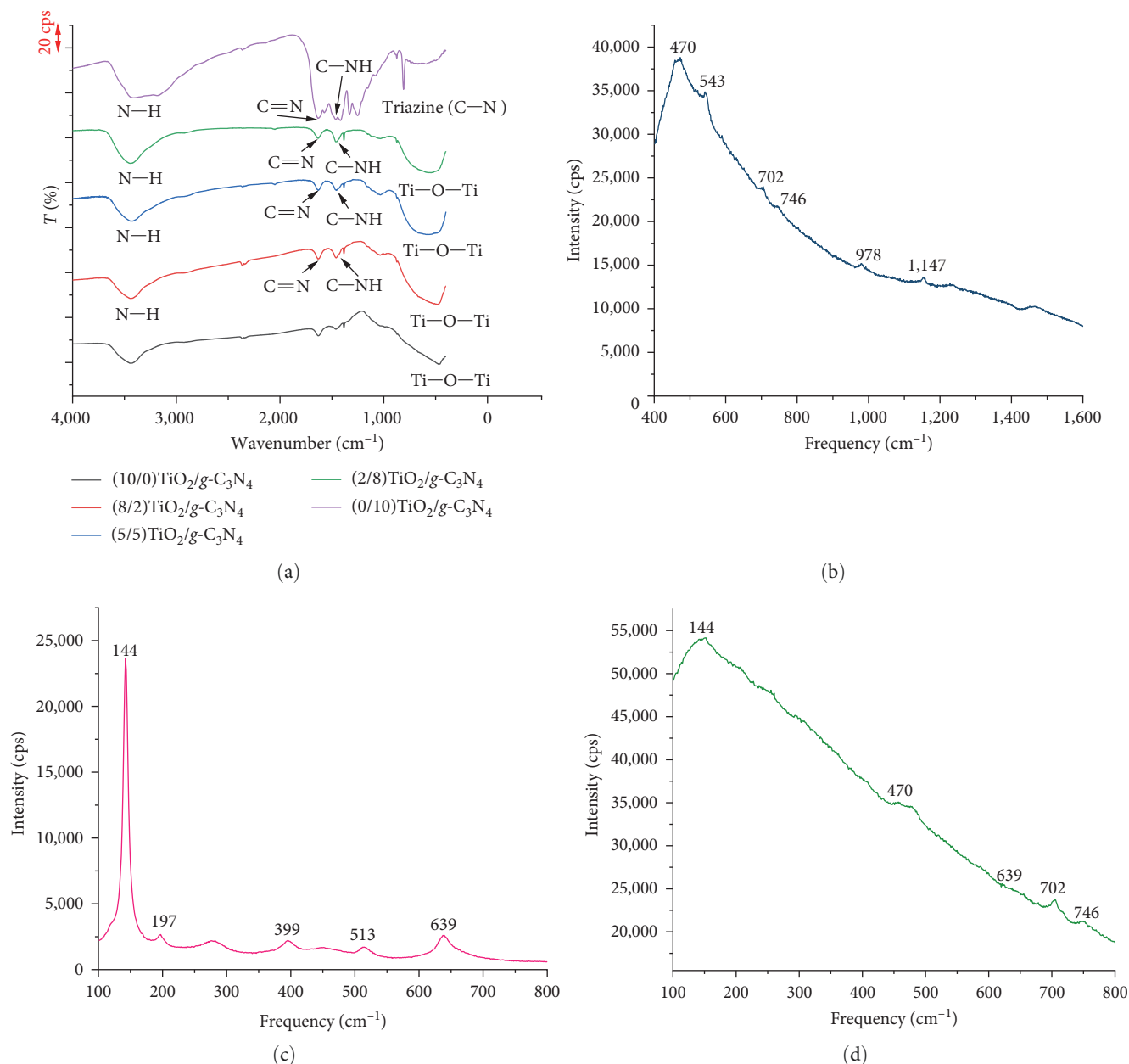


FIGURE 3: FTIR spectra of $g\text{-C}_3\text{N}_4$, TiO_2 , and $\text{TiO}_2/g\text{-C}_3\text{N}_4$ composites (a) and the Raman spectra of (b) $g\text{-C}_3\text{N}_4$, (c) TiO_2 , and (d) $\text{TiO}_2/g\text{-C}_3\text{N}_4$ composites.

the Ti–O–Ti bonds at 470 cm^{-1} are typical for TiO_2 [21]. The vibrations of both $g\text{-C}_3\text{N}_4$ and TiO_2 in the FTIR spectra of $\text{TiO}_2/g\text{-C}_3\text{N}_4$ composites again confirm the composite formation between $g\text{-C}_3\text{N}_4$ and TiO_2 .

The $(2/8)\text{TiO}_2/g\text{-C}_3\text{N}_4$ composite was also characterized from Raman spectra (Figure 3(b)–3(d)). The characteristic peaks of $g\text{-C}_3\text{N}_4$ at 470 , 543 , 702 , 746 , 978 , and $1,147\text{ cm}^{-1}$ are observed, which are similar to those as reported by Bai et al. [25]. For TiO_2 , the vibration modes at 144 cm^{-1} (E_g), 197 cm^{-1} (E_g), 399 cm^{-1} (B_{1g}), 513 cm^{-1} (A_{1g}), and 639 cm^{-1} (E_g) belong to anatase [26, 27]. For the $\text{TiO}_2/g\text{-C}_3\text{N}_4$ composite, the vibrations of TiO_2 and $g\text{-C}_3\text{N}_4$ observed in the Raman spectra confirm the coexistence of TiO_2 and $g\text{-C}_3\text{N}_4$.

UV–vis diffuse reflectance spectra were employed to evaluate the bandgap of the material. Compared with pristine TiO_2 , $\text{TiO}_2/g\text{-C}_3\text{N}_4$ displays a significant red shift because of the band alignment of coupled TiO_2 and $g\text{-C}_3\text{N}_4$ (Figure 4(a)). This shift suggests that introducing $g\text{-C}_3\text{N}_4$ into TiO_2 could enhance the visible light absorption available to $\text{TiO}_2/g\text{-C}_3\text{N}_4$. The bandgap of $g\text{-C}_3\text{N}_4$ and $\text{TiO}_2/g\text{-C}_3\text{N}_4$ was estimated from the Tauc equation [28]: $\alpha(h\nu) = A(h\nu - E_g)^{n/2}$, where α is the absorption coefficient; $h\nu$ is the energy of photon; E_g is the bandgap of the semiconductor; and A is the constant. The index n depends on the properties of the transition of semiconductors: $n = 1$ for direct transition and $n = 4$ for indirect transition semiconductors. TiO_2 and $g\text{-C}_3\text{N}_4$ are indirect

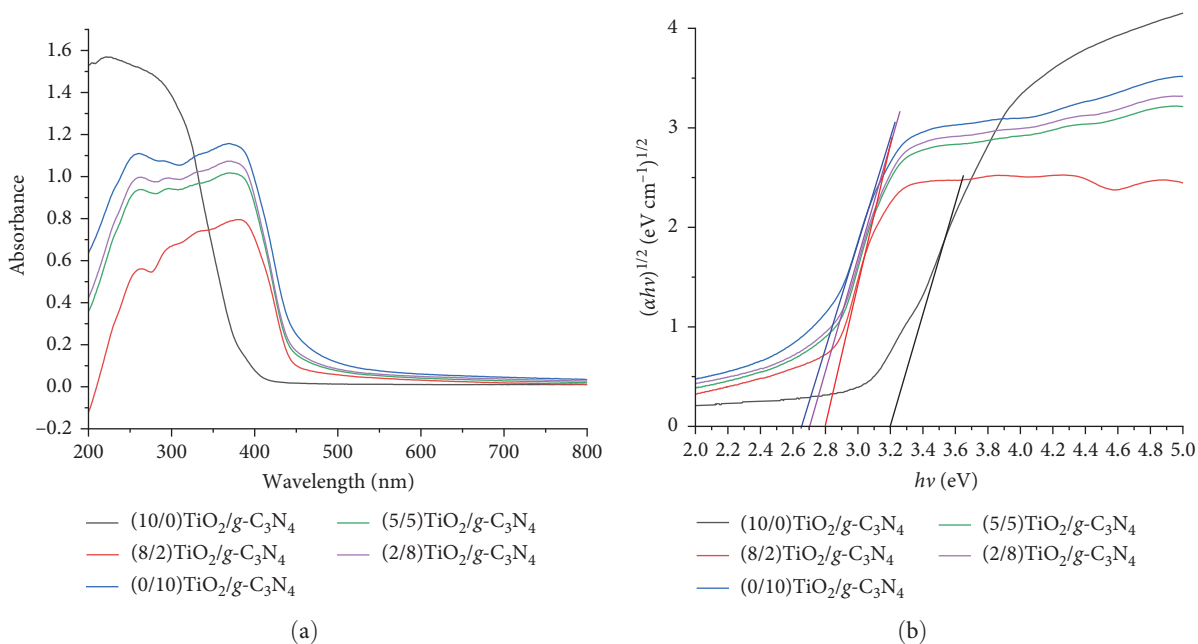


FIGURE 4: (a) UV-vis diffuse reflectance spectra UV-vis DRS; (b) bandgap energy-based Tauc of $g\text{-C}_3\text{N}_4$, TiO_2 , and $\text{TiO}_2/g\text{-C}_3\text{N}_4$ composites.

bandgap semiconductors. Thus, the value of n for $g\text{-C}_3\text{N}_4$, TiO_2 , and $\text{TiO}_2/g\text{-C}_3\text{N}_4$ is 4. The calculated bandgaps are 3.20, 2.80, 2.75, 2.70, and 2.65 eV for (10/0) $\text{TiO}_2/g\text{-C}_3\text{N}_4$, (8/2) $\text{TiO}_2/g\text{-C}_3\text{N}_4$, (5/5) $\text{TiO}_2/g\text{-C}_3\text{N}_4$, (2/8) $\text{TiO}_2/g\text{-C}_3\text{N}_4$, and (0/10) $\text{TiO}_2/g\text{-C}_3\text{N}_4$, respectively (Figure 4(b)). It is possible that $g\text{-C}_3\text{N}_4$, a nitrogen-rich molecule, also acts as a nitrogen source to form $\text{TiO}_{2-x}\text{N}_x$. The substitution of N in the TiO_2 lattice results in a visible light response owing to an additional N level above the TiO_2 VB that triggers the bandgap to narrow to 0.55 eV. These results confirm that the formation of heterojunction between $g\text{-C}_3\text{N}_4$ and TiO_2 could narrow the bandgap of pristine TiO_2 and enhance visible light availability.

The elemental composition in the composite was studied by EDX-mapping. Figure 5 illustrates the EDX-mapping of the (2/8) $\text{TiO}_2/g\text{-C}_3\text{N}_4$ sample. The electron image shows that this sample has a porous structure that agglomerates in large particles of several micrometers (Figure 5(a)). EDX spectrum exhibits the existence of C, N, and Ti elements (Figure 5(b)). Figure 5(c)–5(f) shows that C, N, O, and Ti are evenly dispersed in the material.

The morphology of TiO_2 , $g\text{-C}_3\text{N}_4$, and (2/8) $\text{TiO}_2/g\text{-C}_3\text{N}_4$ is shown in Figure 6. Figure 6(a) shows the layered structure of $g\text{-C}_3\text{N}_4$ with a nanometer stacking that is typical for the C_3N_4 graphite layers. The morphology of TiO_2 consists of titania fibers with a 2×100 nm diameter and irregular sheets around 50–100 nm in diameters. Composite $\text{TiO}_2/g\text{-C}_3\text{N}_4$ (Figure 6(c)) is formed through embroidering the titania fiber and the $g\text{-C}_3\text{N}_4$ layers in a nanoscale, suggesting the formation of the heterojunction interface in the $\text{TiO}_2/g\text{-C}_3\text{N}_4$ composite.

3.1. Visible-Light-Driven Photocatalyst for Methylene Blue (MB) Decomposition

3.1.1. Kinetics of MB Decolorization. Figure 7(a) displays the photocatalytic activity of the $g\text{-C}_3\text{N}_4$, TiO_2 , and $\text{TiO}_2/g\text{-C}_3\text{N}_4$

composites. The experiment was conducted in two stages: adsorption in the dark and photocatalytic decomposition of MB. The adsorption lasted for 40 min to ensure the adsorption/desorption equilibrium, followed by visible-light irradiation for 40 min. It is obvious that the pristine $g\text{-C}_3\text{N}_4$ and TiO_2 possess either low adsorption capacity or poor decolorization, indicating that these materials do not catalyze MB decomposition. The color of the MB solution remains almost unchanged after 40 min of irradiation, suggesting MB is stable under these conditions. The $\text{TiO}_2/g\text{-C}_3\text{N}_4$ composites substantially enhance MB decolorization compared with the components. The MB decolorization rate increases with the increasing amount of $g\text{-C}_3\text{N}_4$ and peaks for the (2/8) $\text{TiO}_2/g\text{-C}_3\text{N}_4$ sample. Therefore, this sample was selected for further experiments.

The leaching of active metal species to the liquid phase was studied by removing the catalyst after 50 min of illumination, and the MB decolorization was studied. It was found that, although illumination continued for up to 120 min (Figures 7(b) and 7(c)), the MB decolorization did not occur in the absence of the catalyst. Only a small amount of leaching titanium was also detected in the supernatant ($0.336 \text{ mg}\cdot\text{L}^{-1}$) by ICP analysis. This fact confirms that (2/8) $\text{TiO}_2/g\text{-C}_3\text{N}_4$ is a heterogeneous catalyst in MB photocatalytic degradation.

The kinetics of MB decomposition is shown in Figure 7(d). The process was conducted in two stages, as described above. The (2/8) $\text{TiO}_2/g\text{-C}_3\text{N}_4$ sample exhibits adsorption equilibrium after around 40 min with an equilibrium adsorption efficiency of $\sim 8\%$ – 10% , depending on the initial concentration. The higher the MB concentration, the larger the adsorption capacity is because of the increasing driving force. The kinetics of photocatalytic decomposition is widely described by using the Langmuir and Hinshelwood (L–H) mechanism [29–31]. In this case, MB adsorption on the catalyst surface follows the Langmuir isotherm, and the adsorption

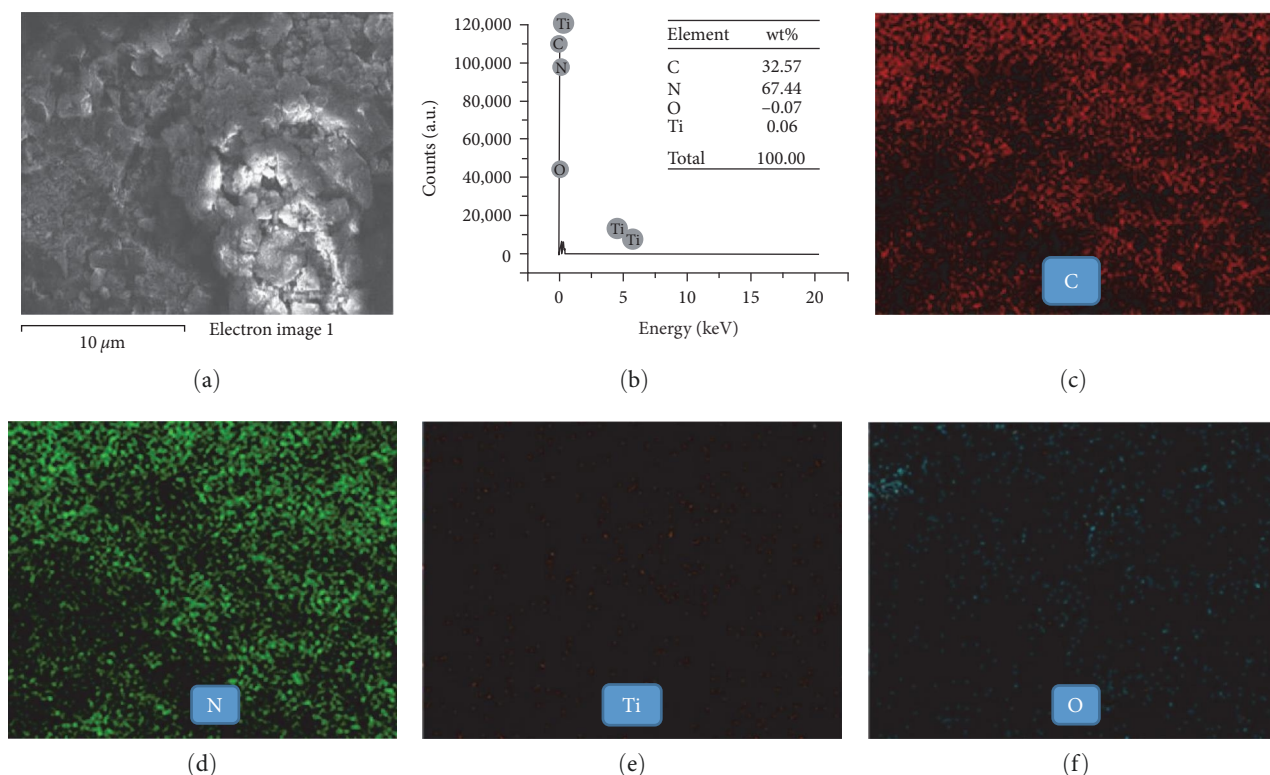


FIGURE 5: EDX-mapping of (2/8) $\text{TiO}_2/\text{g-C}_3\text{N}_4$: electron image (a); EDX spectrum (b); C element (c); N element (d); Ti element (e); O element (f).

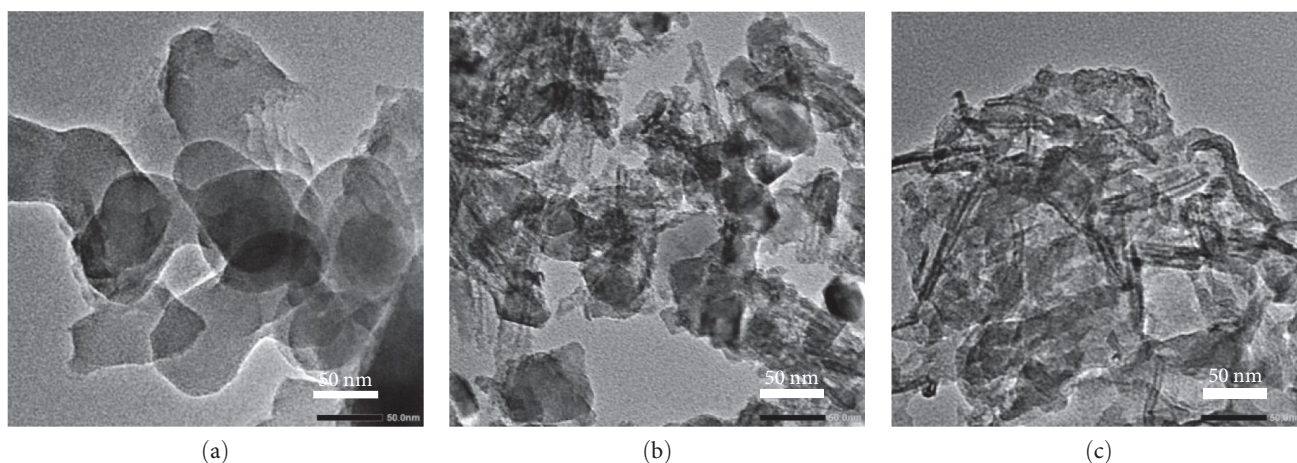
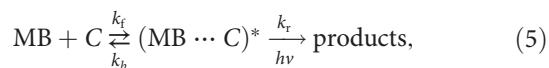


FIGURE 6: TEM images of (a) $\text{g-C}_3\text{N}_4$; (b) TiO_2 ; (c) $\text{TiO}_2/\text{g-C}_3\text{N}_4$ composites.

equilibrium maintains during the photocatalytic reaction, that is, the adsorption rate is larger than the reaction rate of the electrons or holes, which is the rate-determining step. The reactions and kinetics equation are expressed as follows:



$$\ln\left(\frac{C_{0e}}{C}\right) = k_{\text{app}}t, \quad (6)$$

where k_f and k_b are the forward and backward adsorption rate coefficients; k_r is the rate constant of the photocatalytic reaction; C_{0e} (ppm) is the MB concentration at the

equilibrium of dark adsorption; and k_{app} (min^{-1}) is the apparent rate constant.

The value of k_{app} can be obtained from the linear plot of $\ln C_{0e}/C$ vs. t . It was found that the fitted lines of $\ln C_{0e}/C$ against irradiation time exhibit high linearity ($R^2 = 0.9679$), and these values indicate that the MB photodegradation apparently fits well with pseudo-first-order kinetics [32]. The pseudo rate constant at different MB concentrations is listed in Table 2. A comparison of k_{app} with those of previous reports is also presented. It was found that the rate constant of MB decolorization in this paper is a bit higher than those of previous reports, confirming the advantage of synthesizing TiO_2 -based materials from water-soluble titanium complexes.

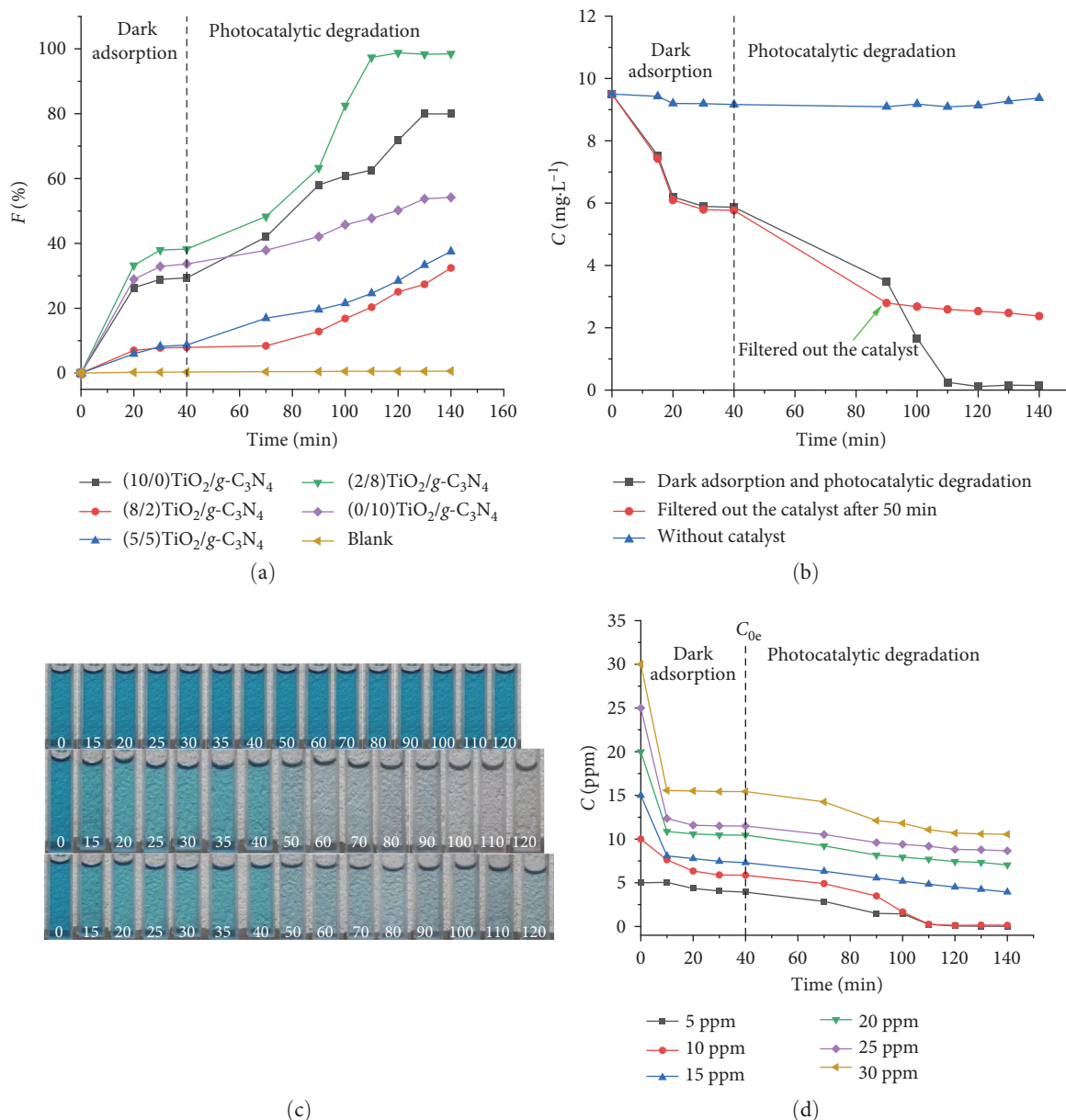


FIGURE 7: (a) Decomposition of MB on several catalysts; (b) catalytic leaching experiments; (c) variation of decolorization in the leaching experiment; (d) kinetics of MB decomposition on (2/8) TiO₂/g-C₃N₄ at different initial concentrations (conditions: $V = 100$ mL, $m_{\text{catalyst}} = 0.02$ g, light-illumination time: 100 min, ambient temperature).

3.1.2. Effect of pH and Some Scavengers on MB Decomposition. The pH effect of dark adsorption and photocatalytic decomposition of MB is shown in Figure 8(a). When $\text{pH} > 3.8$ (pK_a of MB 3.8 [40]), MB is positively charged. The pH_{PZC} value of TiO₂/g-C₃N₄ determined with the pH shift method is 7.4. At pH less than pH_{PZC} , the material's surface carries a positive charge because of protonation. The MB degradation efficiency increases gradually with pH from 4 to 10. When $\text{pH} > 7.4$, the electrostatic interaction between the material's negatively charged surface and positively charged MB causes decolorization efficiency to increase.

The results of free radical scavenging experiments are shown in Figure 8(b). The experiments were conducted to

determine the free radicals formed during irradiation, causing MB decomposition. The three free radical scavengers used in the research are based on Tu et al. [41]: potassium iodide to capture h^+ , isopropanol to capture $\cdot\text{OH}$, and benzoquinone to capture $\text{O}_2^{\cdot-}$. The results indicate that benzoquinone significantly reduces MB decolorization, followed by isopropanol and potassium iodide, indicating that free radicals play an essential role in the MB degradation in the following order: $\text{O}_2^{\cdot-} > \cdot\text{OH} > \text{h}^+$.

3.1.3. Photocatalytic Degradation Pathway of MB. The UV-vis absorption spectrum of MB solutions is shown in Figure 8(c). The absorption peaks at 245 and 292 nm correspond to the excitation of π -electrons from the $\pi-\pi^*$

TABLE 2: Apparent rate constant of MB decolorization in this work and from the literature at different concentrations for MB.

Catalysts	Light source (nm, power)	Degradation percentage (%) / time (min)	C_0 (ppm) / volume (mL) / m_{catalyst} (mg)	k_{app} (min^{-1})	References
$\text{Fe}_3\text{O}_4/\text{MIL-101}$	<400, 60 W	95/650	10/100/50	0.030	[33]
$\text{CeO}_2/\text{TiO}_2$	<400, 250 W	100/120	15/100/80	0.034	[34]
$\beta\text{-AgVO}_3$	Sunlight	75/120	20/50/20	0.250	[35]
ZnO@GO	365, 40 W	98.5/15	20/50/10	0.254	[36]
$\text{TiO}_2/\text{diazonium}/\text{GO}$	<400, 75 W	100/120	20/100/100	0.160	[37]
ZnO	≥ 400 , 300 W	–	200/50/50	0.002	[38]
$\text{Al-Fe}/\text{ZnO}$	≥ 400 , 300 W	90/75	200/50/50	0.014	[38]
TiO_2	420, 500 W	N/A	10/100/100	0.001	[39]
$g\text{-C}_3\text{N}_4$	420, 500 W	N/A	10/100/100	0.002	[39]
$g\text{-C}_3\text{N}_4/\text{TiO}_2/\text{diatomite}$	420, 500 W	83/360	10/100/100	0.001	[39]
$\text{TiO}_2/g\text{-C}_3\text{N}_4$	<400, 160 W	98.5/100	5/100/20	0.099	This work
			10/100/20	0.071	
			20/100/20	0.002	

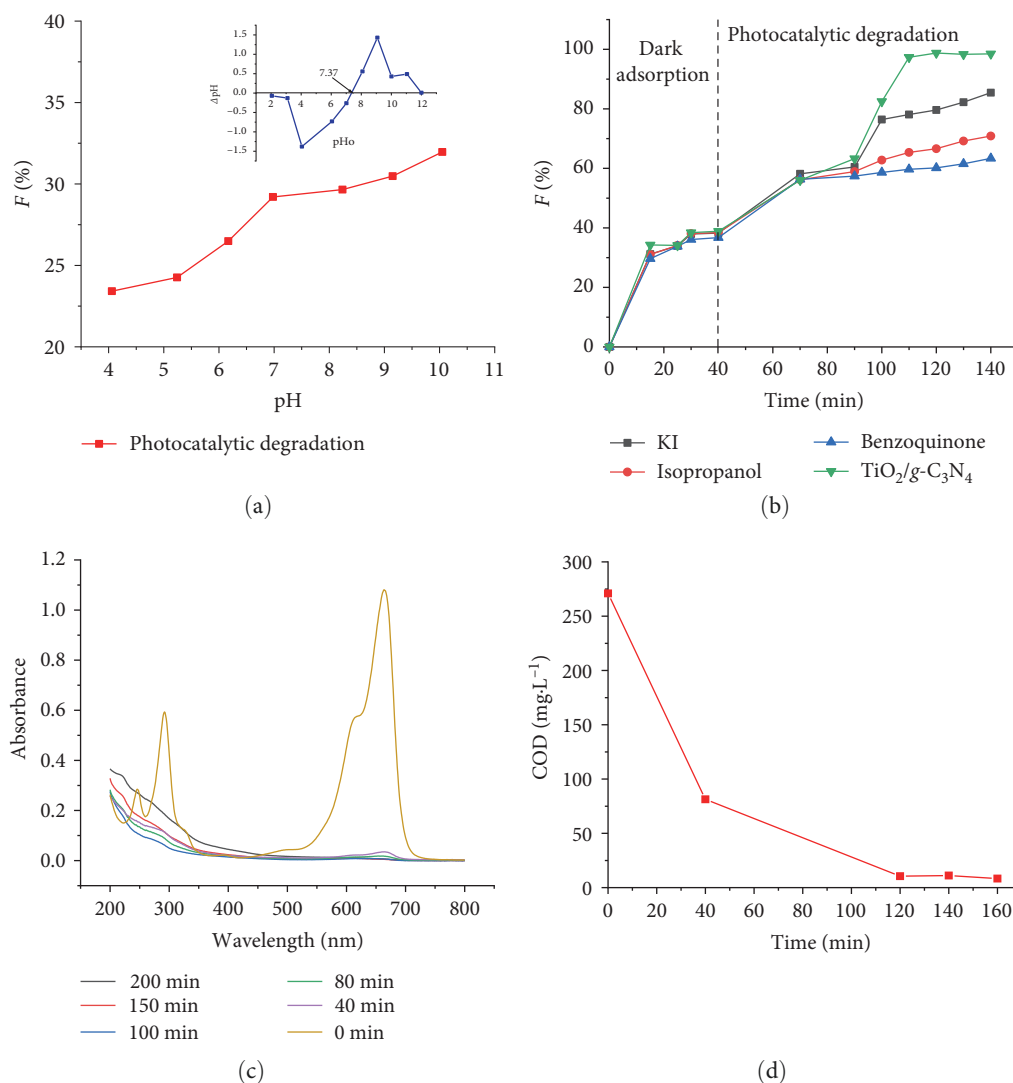


FIGURE 8: (a) Effect of pH on MB decolorization; the inset presents the estimation for point of zero charge (pH_{PZC}) of $(2/8)\text{TiO}_2/g\text{-C}_3\text{N}_4$; (b) yield of MB decolorization with present of the scavengers using $(2/8)\text{TiO}_2/g\text{-C}_3\text{N}_4$ catalyst (conditions: $V = 100$ mL, $C_{0(\text{MB})} = 10$ ppm, $m_{\text{catalyst}} = 0.02$ g, $V_{\text{scavenger}} = 20$ mL, illumination time: 120 min, ambient temperature); (c) UV-vis spectra; (d) kinetics of disappearance of chemical oxygen demand (COD) on $(2/8)\text{TiO}_2/g\text{-C}_3\text{N}_4$ (conditions: c) $V = 100$ mL, $C_{0(\text{MB})} = 10$ ppm, $m_{\text{catalyst}} = 0.02$ g, illumination time: 200 min; (d) $V = 100$ mL, $C_{0(\text{MB})} = 500$ ppm, $m_{\text{catalyst}} = 1.00$ g, illumination time: 120 min, ambient temperature).

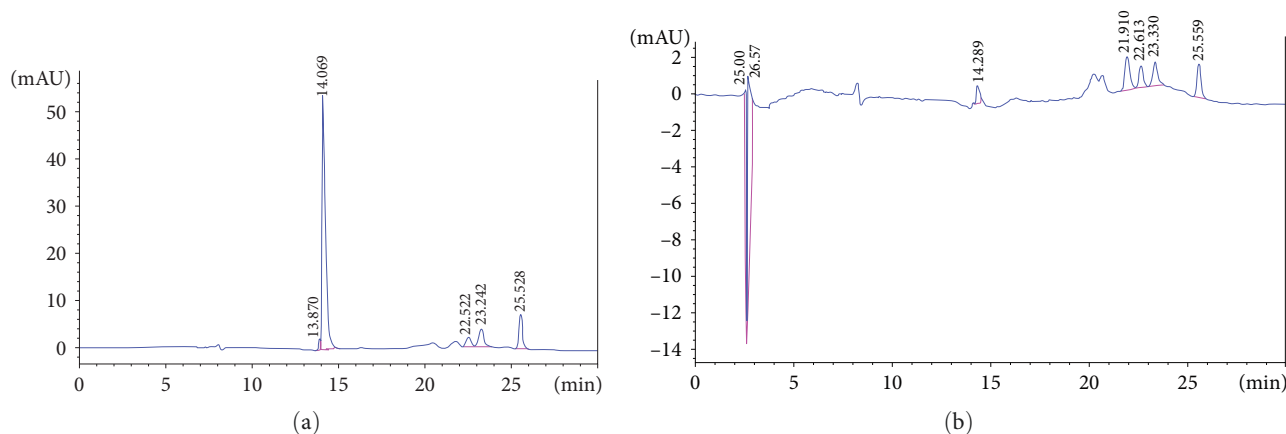


FIGURE 9: (a) HPLC diagram of MB before; (b) after 100 min photodegradation (conditions: $V = 250$ mL, $C_{0(\text{MB})} = 10$ ppm, $m_{\text{catalyst}} = 0.05$ g, illumination time: 100 min).

interaction in the benzene ring, while those at 615 and 664 nm are assigned to the benzene ring and the heteropolycyclic aromatic linkage [42]. The maximum absorption occurs at 664 nm. The intensity of the adsorption peaks decreases with increasing illumination time, and the color of the MB solution almost disappears after 100 min of illumination. This decolorization reveals that the MB structure was destroyed during illumination. The mineralization of carbons is also evidenced by the COD values, as shown in Figure 8(d). COD gradually decreases from an initial 271 to $11.1 \text{ mg}\cdot\text{L}^{-1}$ after 100 min of irradiation and $8.3 \text{ mg}\cdot\text{L}^{-1}$ after 120 min. This decolorization is associated with the aromatic ring opening with the transient formation of carboxylic acids, followed by the evolution of CO_2 according to the “photo-Kolbe” reaction: $\text{R-COO}^- + \text{h}^+ \longrightarrow \text{R}^\bullet + \text{CO}_2$. Methylene blue is broken down into harmless or less harmful substances, such as carbon dioxide (CO_2) and water (H_2O), via certain intermediates.

The degradation of MB was also studied quantitatively by using HPLC before and after degradation. The peak area reveals that an insignificant amount of MB remains after the 100 min illumination (only 3.7% remains (Figure 9)).

The intermediate compounds were identified by using liquid chromatography–mass spectrometry (LC–MS), as shown in Figure 10. Based on the mass/charge ratio (m/z) in the mass spectra, we proposed the compounds and their structural formulas (Scheme 2). The signal at m/z of 284 presents before degradation is assigned to MB. Then, the cleavage of each methyl group on amine groups, in turn, leads to the formation of Azure B, Azure A, and thionin, with m/z of 268, 252, and 225, respectively (Figure 10(a)–10(e)). These products result from the reduction of the methyl group in the MB molecule via photocatalytic degradation [35, 43]. The peak at 1.8 min (Figure 10(f)) corresponding to m/z 192 is attributed to $\text{HO-C}_6\text{H}_3\text{-SO}_3\text{H}(\text{NH}_3^+)$. Accordingly, the decomposition is due to the cleavage of the bonds in the $\text{C-S}^+=\text{C}$ and $\text{C-N}=\text{C}$ functional groups. The $\text{C-S}^+=\text{C}$ group is attacked by HO^\bullet radicals and oxidized to the $\text{C-S}(\text{=O})\text{-C}$ sulfoxide group, causing the formation of a central imino group ($-\text{NH}$) at the para-position of the middle aromatic ring.

The H atoms for the formation of C-H and N-H bonds may result from the deprotonation by photogenerated electrons to form H^- radicals [44]. The saturation of the two amino groups by H^- radicals produces substituted aniline. Then, the amino group can be replaced by an OH^- radical, forming the corresponding phenol and releasing an NH_2^- radical producing NH_3 and ammonium ions. The sulfoxide group can be attacked by HO^\bullet radicals for the second time to produce sulfone. At the same time, the HO^\bullet radicals cause ring cleavage; then, the sulfone group can be further attacked by HO^\bullet radicals to produce sulfonic acid. The peak at 2.1 min (Figure 10(g)) corresponding to m/z of 164 is assigned to $(\text{HO})_2\text{C}_6\text{H}_3\text{-N}(\text{CH}_3)\text{-CHO}$. Accordingly, the first step is due to the cleavage of the bonds in $\text{C-S}^+=\text{C}$ and $\text{C-N}=\text{C}$ in Azure B, which are then attacked by HO^\bullet radicals to form NH_2 and NH groups. They are further attacked by HO^\bullet radicals and form $-\text{OH}$ groups in phenol, and the $-\text{CH}_3$ group in $\text{N}(\text{CH}_3)_2$ forms the $-\text{CHO}$ group. Thus, the obtained structure is consistent with the structure of the fragment with m/z of 167, as proposed by Houas et al. [44]. The peak at 2.7 min (Figure 10(h)) corresponding to m/z of 137 has the proposed structure as $(\text{HO})_2\text{C}_6\text{H}_3\text{-NH-CH}_3$. Accordingly, the $-\text{CHO}$ group can be attacked by HO^\bullet radicals to form the $-\text{COOH}$ group. Then, the N-COOH group is attacked by h^+ to form N^\bullet , and it combines with H^+ to form the $-\text{NH-}$ group.

3.1.4. Mechanism of MB decomposition. The valence band (VB) and CB potential edges of $g\text{-C}_3\text{N}_4$ and TiO_2 were calculated according to the equations proposed by Xu and Schoonen [45] and Lin et al. [46] as follows:

$$E_{\text{CB}} = \chi - E_e - 0.5 \cdot E_g, \quad (7)$$

$$E_{\text{VB}} = E_g + E_{\text{CB}}, \quad (8)$$

where E_{CB} is the CB edge energy, E_{VB} is the VB edge energy, χ is the electronegativity ($\chi = 4.73$ eV for $g\text{-C}_3\text{N}_4$ and $\chi = 5.81$ eV for TiO_2 [45]), E_e is the free energy of electrons with respect to the NHE ($E_e = 4.5$ eV [47]), and E_g is the bandgap energy of the semiconductor.

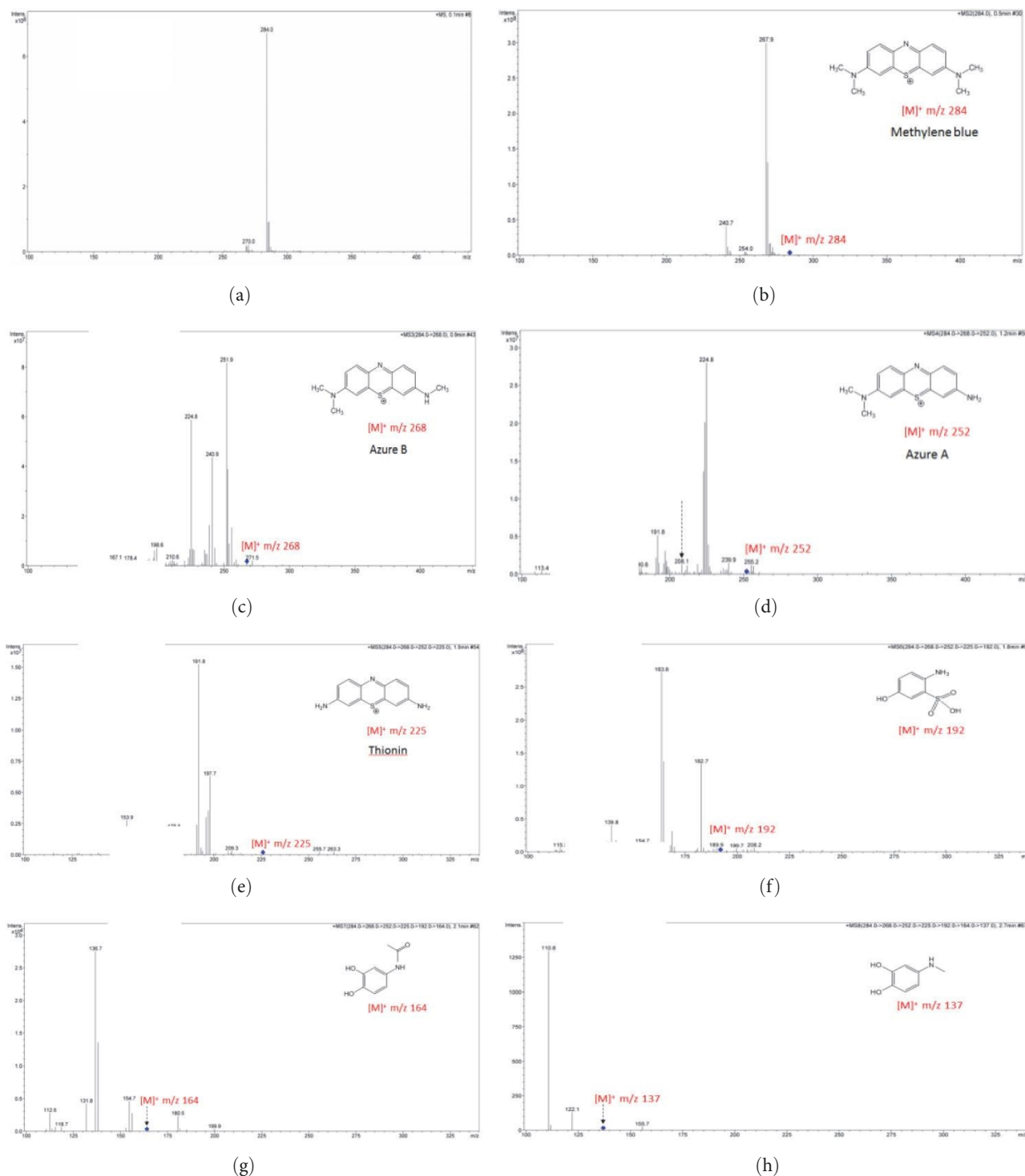
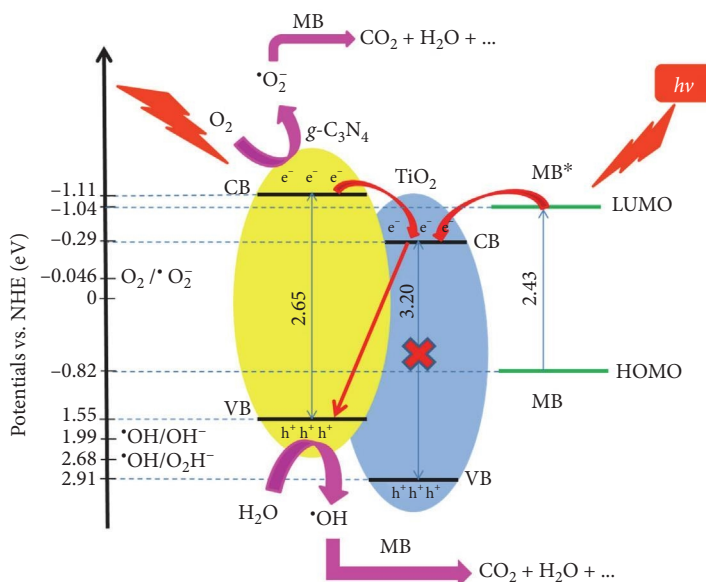
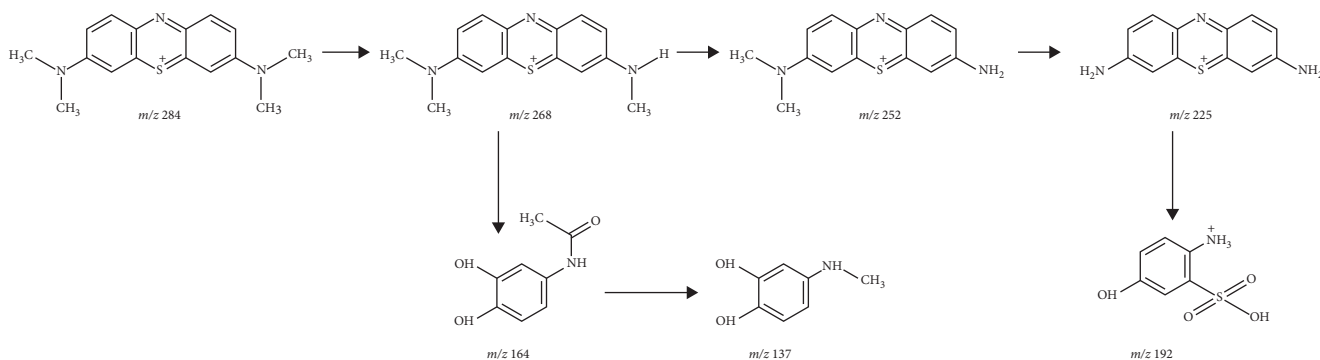


FIGURE 10: MS of degradation pathway of MB at 0.1 (a); 0.5 (b); 0.9 (c); 1.2 (d); 1.5 (e); 1.8 (f); 2.1 (g); 2.7 (h) min.

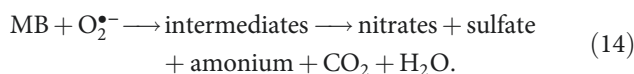
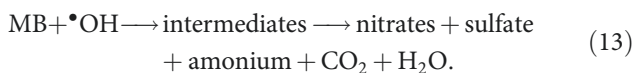
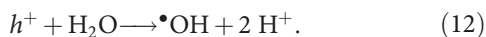
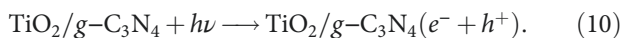
The values of E_{CB} and E_{VB} for $g\text{-C}_3\text{N}_4$, calculated from Equations (7) and (8), are -1.11 and 1.55 eV, and those for TiO_2 are -0.29 and 2.91 eV, respectively. The position of the edge energy of $g\text{-C}_3\text{N}_4$ and TiO_2 is shown in Scheme 3. First, MB is adsorbed by $\text{TiO}_2/g\text{-C}_3\text{N}_4$, and its aromatic rings interact with $g\text{-C}_3\text{N}_4$ or TiO_2 on the surface via $\pi\text{-}\pi$ bonding [48]. Under visible-light illumination, the MB molecule can be excited, and the photoelectrons in HOMO of MB (-0.82 eV)

migrate to LUMO of MB (-1.04 eV) (Equation (9)) [49]. These photoelectrons could transfer to the CB of TiO_2 . The VB electrons of $g\text{-C}_3\text{N}_4$ would be excited, and the photoelectron-hole pairs are, thus, generated. These photoelectrons have a chance to transfer to the CB of TiO_2 , which enhances the photoelectron-hole separation (Equation (10)). The electrons and holes could react with oxygen and water to form free radicals (Equations (11) and (12)). They, in



turn, can decompose MB to different products with decreasing molecular mass under prolonged light illumination. MB can be completely mineralized to inorganic substances (CO_2 , H_2O , Cl^- , NO_3^- , SO_4^{2-} , and NH_4^+), similar to what was reported by Houas et al. [44].

The following photocatalytic degradation mechanism for MB decomposition on the $\text{TiO}_2/\text{g-C}_3\text{N}_4$ catalyst is illustrated as follows:



3.2. Recyclability of $\text{TiO}_2/\text{g-C}_3\text{N}_4$. The catalyst's reuse after a catalytic reaction is a critical requirement besides its high catalytic activity. The used catalyst was regenerated by calcining in the nitrogen atmosphere at 500°C for 3 hr. The SEM observation of the catalyst after the dark adsorption following the dye degradation is shown in Figures 11(a) and 11(b). As seen from the figure, the particles of the catalyst present the large agglomerates resulted in the combination of fine particles and dyes molecules. After the third recycle, fine particles are separated clearly indicating that the MB dyes are removed from the surface of $(2/8)\text{TiO}_2/\text{g-C}_3\text{N}_4$ due to the photocatalytic degradation of MB. The MB decomposition efficiency after three recycling is found as 98.5%, 93.0%, 87.5%, and 82.5%. It is obvious that the efficiency decreases gradually after each recycling. It drops only around 6% after three recyclings, compared with the first reaction. The XRD patterns of the catalyst remain

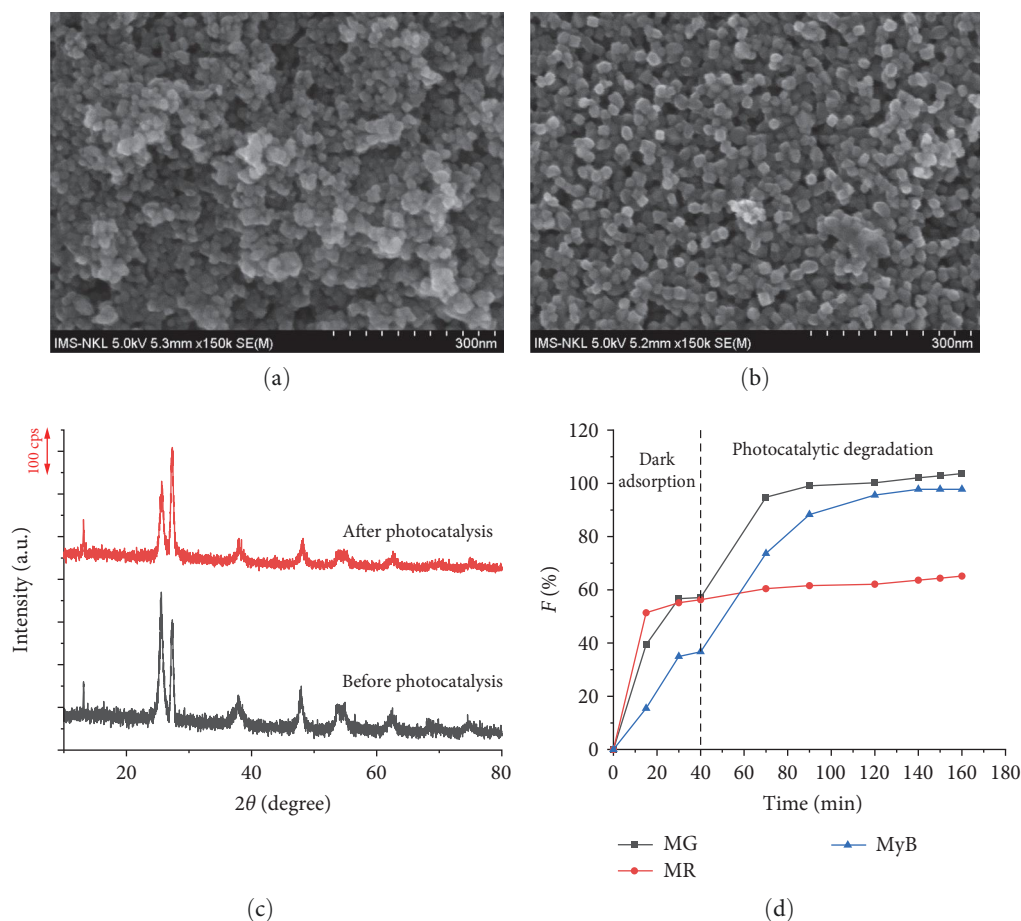


FIGURE 11: SEM images of the composite: (a) after dye adsorption; (b) following dye degradation; (c) the XRD patterns of initial and reused catalysts; (d) degradation of MG, MR, and MyB by $(2/8)\text{TiO}_2/g\text{-C}_3\text{N}_4$ (conditions: $V = 100\text{ mL}$, $C_0(\text{MG}; \text{MR}; \text{MyB}) = 10\text{ ppm}$, $m_{\text{catalyst}} = 0.02\text{ g}$, illumination time: 120 min, ambient temperature).

unchanged, indicating that the catalyst is stable and promising for treating dyes wastewaters (Figure 11(c)).

3.3. Photocatalytic Activity $\text{TiO}_2/g\text{-C}_3\text{N}_4$ for Other Dyes. To confirm the photochemical degradation ability of $\text{TiO}_2/g\text{-C}_3\text{N}_4$ materials for other dyes under visible illumination, we also conducted other experiments with malachite green (MG), methyl blue (MyB), and methyl red (MR). The assessment of color degradation was based on the change in the main absorption peak's intensity at λ_{max} of 617 nm for MG, 607 nm for MyB, and 521 nm for MR. Figure 11(d) shows that the $\text{TiO}_2/g\text{-C}_3\text{N}_4$ material exhibits high catalytic ability in the decomposition of these organic dyes, especially the cationic ones. The photochemical degradation efficiency of MG with the cationic configuration is 100% after 80 min of illumination. Methyl blue with the anionic configuration decomposes by 97.8% after 100 min, and MR with the neutral configuration decomposes by 65.9% after 120 min. This result shows that $\text{TiO}_2/g\text{-C}_3\text{N}_4$ is possibly a photocatalyst working in the visible light region to decompose organic dyes in aqueous media.

4. Conclusion

A novel and facile approach to the in situ synthesis of $\text{TiO}_2/g\text{-C}_3\text{N}_4$ nanoparticles with heterostructures and enhanced

photocatalytic activity was demonstrated. The composites were synthesized from a homogeneous mixture of melamine and a water-soluble titanium (IV) complex, which initiates an intimate interfacial contact between TiO_2 nanoparticles and $g\text{-C}_3\text{N}_4$ nanosheets with a relatively large surface area. The obtained catalyst exhibits excellent catalytic activity toward methylene blue decomposition. The dye was degraded via a free radical mechanism in which the radical activity followed the order $\text{O}_2^{\bullet-} > \text{OH} > \text{h}^+$. First, methylene blue was degraded by opening its central aromatic rings, then the oxidation of their subsequent metabolites, and finally, the evolution of CO_2 . In addition, $\text{TiO}_2/g\text{-C}_3\text{N}_4$ also exhibited efficient photocatalytic degradation toward other dyes, such as malachite green, methyl red, and methyl blue. The $\text{TiO}_2/g\text{-C}_3\text{N}_4$ material is a promising catalyst for treating diluted wastewater in textile industries.

Data Availability

The data used to support the findings of this study are available from the corresponding author upon request.

Conflicts of Interest

The authors declare that they have no conflicts of interest.

Funding

This work was financially supported by Hue University, Vietnam, under project code DHH 2021-04-151 and Van Lang University, Vietnam.

Acknowledgments

The authors (Nguyen Thi Thanh Tu and Dang Thi Ngoc Hoa) thank the financial support from Hue University and Van Lang University.

References

- [1] S. C. Yan, Z. S. Li, and Z. G. Zou, "Photodegradation performance of $g\text{-C}_3\text{N}_4$ fabricated by directly heating melamine," *Langmuir*, vol. 25, no. 17, pp. 10397–10401, 2009.
- [2] X. Wang, K. Maeda, A. Thomas et al., "A metal-free polymeric photocatalyst for hydrogen production from water under visible light," *Nature Materials*, vol. 8, pp. 76–80, 2009.
- [3] L. Shi, F. Wang, J. Zhang, and J. Sun, "Onion-like carbon modified porous graphitic carbon nitride with excellent photocatalytic activities under visible light," *Ceramics International*, vol. 42, no. 16, pp. 18116–18123, 2016.
- [4] A. Piątkowska, M. Janus, K. Szymański, and S. Mozia, "C-, N- and S-doped TiO_2 photocatalysts: a review," *Catalysts*, vol. 11, no. 1, Article ID 144, 2021.
- [5] C. M. Teh and A. R. Mohamed, "Roles of titanium dioxide and ion-doped titanium dioxide on photocatalytic degradation of organic pollutants (phenolic compounds and dyes) in aqueous solutions: a review," *Journal of Alloys and Compounds*, vol. 509, no. 5, pp. 1648–1660, 2011.
- [6] K. Nagaveni, M. S. Hegde, N. Ravishankar, G. N. Subbanna, and G. Madras, "Synthesis and structure of nanocrystalline TiO_2 with lower band gap showing high photocatalytic activity," *Langmuir*, vol. 20, no. 7, pp. 2900–2907, 2004.
- [7] A. D. Vital-Grappin, M. C. Ariza-Tarazona, V. M. Luna-Hernández et al., "The role of the reactive species involved in the photocatalytic degradation of HDPE microplastics using C, N- TiO_2 powders," *Polymers*, vol. 13, no. 7, Article ID 999, 2021.
- [8] N. Kaur, A. Verma, I. Thakur, and S. Basu, "In-situ dual effect of Ag-Fe- TiO_2 composite for the photocatalytic degradation of Ciprofloxacin in aqueous solution," *Chemosphere*, vol. 276, Article ID 130180, 2021.
- [9] R. Acharya and K. Parida, "A review on $\text{TiO}_2/g\text{-C}_3\text{N}_4$ visible-light-responsive photocatalysts for sustainable energy generation and environmental remediation," *Journal of Environmental Chemical Engineering*, vol. 8, no. 4, Article ID 103896, 2020.
- [10] Y. Liu, S. Wu, J. Liu, S. Xie, and Y. Liu, "Synthesis of $g\text{-C}_3\text{N}_4/\text{TiO}_2$ nanostructures for enhanced photocatalytic reduction of U(VI) in water," *RSC Advances*, vol. 11, no. 8, pp. 4810–4817, 2021.
- [11] H. Zhang, F. Liu, H. Wu, X. Cao, J. Sun, and W. Lei, "In situ synthesis of $g\text{-C}_3\text{N}_4/\text{TiO}_2$ heterostructures with enhanced photocatalytic hydrogen evolution under visible light," *RSC Advances*, vol. 7, no. 64, pp. 40327–40333, 2017.
- [12] M. A. Alcudia-Ramos, M. O. Fuentes-Torres, F. Ortiz-Chi et al., "Fabrication of $g\text{-C}_3\text{N}_4/\text{TiO}_2$ heterojunction composite for enhanced photocatalytic hydrogen production," *Ceramics International*, vol. 46, no. 1, pp. 38–45, 2020.
- [13] M. Kakihana, M. Kobayashi, K. Tomita, and V. Petrykin, "Application of water-soluble titanium complexes as precursors for synthesis of titanium-containing oxides via aqueous solution processes," *Bulletin of the Chemical Society of Japan*, vol. 83, no. 11, pp. 1285–1308, 2010.
- [14] Q. D. Truong, L. X. Dien, D.-V. N. Vo, and T. S. Le, "Controlled synthesis of titania using water-soluble titanium complexes: a review," *Journal of Solid State Chemistry*, vol. 251, pp. 143–163, 2017.
- [15] T. T. L. Chau, D. Q. T. Le, H. T. Le, C. D. Nguyen, L. V. Nguyen, and T.-D. Nguyen, "Chitin liquid-crystal-templated oxide semiconductor aerogels," *ACS Applied Materials & Interfaces*, vol. 9, no. 36, pp. 30812–30820, 2017.
- [16] Q. T. D. Le, V. C. Truong, and P. A. Do, "The effect of TiO_2 nanotubes on the sintering behavior and properties of PZT ceramics," *Advances in Natural Sciences: Nanoscience and Nanotechnology*, vol. 2, no. 2, Article ID 025013, 2011.
- [17] G. Schwarzenbach, J. Muehlebach, and K. Mueller, "Peroxo complexes of titanium," *Inorganic Chemistry*, vol. 9, no. 11, pp. 2381–2390, 1970.
- [18] H. Dai, S. Zhang, G. Xu et al., "Highly photoactive heterojunction based on $g\text{-C}_3\text{N}_4$ nanosheets decorated with dendritic zinc (II) phthalocyanine through axial coordination and its ultra-sensitive enzyme-free sensing of choline," *RSC Advances*, vol. 4, no. 102, pp. 58226–58230, 2014.
- [19] R. Hao, G. Wang, C. Jiang, H. Tang, and Q. Xu, "In situ hydrothermal synthesis of $g\text{-C}_3\text{N}_4/\text{TiO}_2$ heterojunction photocatalysts with high specific surface area for Rhodamine B degradation," *Applied Surface Science*, vol. 411, pp. 400–410, 2017.
- [20] L. Lu, G. Wang, M. Zou, J. Wang, and J. Li, "Effects of calcining temperature on formation of hierarchical $\text{TiO}_2/g\text{-C}_3\text{N}_4$ hybrids as an effective Z-scheme heterojunction photocatalyst," *Applied Surface Science*, vol. 441, pp. 1012–1023, 2018.
- [21] Z. Lin, B. Yu, and J. Huang, "Cellulose-derived hierarchical $g\text{-C}_3\text{N}_4/\text{TiO}_2$ -nanotube heterostructured composites with enhanced visible-light photocatalytic performance," *Langmuir*, vol. 36, no. 21, pp. 5967–5978, 2020.
- [22] B. Zhang, X. He, X. Ma et al., "In situ synthesis of ultrafine TiO_2 nanoparticles modified $g\text{-C}_3\text{N}_4$ heterojunction photocatalyst with enhanced photocatalytic activity," *Separation and Purification Technology*, vol. 247, Article ID 116932, 2020.
- [23] H. Shi, J. Du, J. Hou et al., "Solar-driven CO_2 conversion over Co^{2+} doped 0D/2D $\text{TiO}_2/g\text{-C}_3\text{N}_4$ heterostructure: insights into the role of Co^{2+} and cocatalyst," *Journal of CO_2 Utilization*, vol. 38, pp. 16–23, 2020.
- [24] N. Lu, C. Wang, B. Sun, Z. Gao, and Y. Su, "Fabrication of TiO_2 -doped single layer graphitic- C_3N_4 and its visible-light photocatalytic activity," *Separation and Purification Technology*, vol. 186, pp. 226–232, 2017.
- [25] X. Bai, L. Wang, Y. Wang, W. Yao, and Y. Zhu, "Enhanced oxidation ability of $g\text{-C}_3\text{N}_4$ photocatalyst via C_{60} modification," *Applied Catalysis B: Environmental*, vol. 152–153, pp. 262–270, 2014.
- [26] A. G. Ilie, M. Scarisoareanu, I. Morjan, E. Dutu, M. Badiceanu, and I. Mihailescu, "Principal component analysis of Raman spectra for TiO_2 nanoparticle characterization," *Applied Surface Science*, vol. 417, pp. 93–103, 2017.
- [27] X. Chen and S. S. Mao, "Titanium dioxide nanomaterials: synthesis, properties, modifications, and applications," *Chemical Reviews*, vol. 107, no. 7, pp. 2891–2959, 2007.
- [28] J. Zhang, W. Yu, J. Liu, and B. Liu, "Illustration of high-active Ag_2CrO_4 photocatalyst from the first-principle calculation of electronic structures and carrier effective mass," *Applied Surface Science*, vol. 358, Part A, pp. 457–462, 2015.
- [29] A. Amalraj and A. Pius, "Photocatalytic degradation of alizarin red S and bismarck brown R using TiO_2 photocatalyst,"

- Journal of Chemistry & Applied Biochemistry*, vol. 1, no. 1, Article ID 105, 2014.
- [30] S. Khezrianjoo and H. D. Revanasiddappa, “Langmuir-hinshelwood kinetic expression for the photocatalytic degradation of metanil yellow aqueous solutions by ZnO catalyst,” *Chemical Sciences Journal*, vol. 2012, no. 2012, pp. 1–7, 2012.
- [31] A. Phuruangrat, P.-O. Keereesaensuk, K. Karthik et al., “Synthesis of Ag/Bi₂MoO₆ nanocomposites using NaBH₄ as reducing agent for enhanced visible-light-driven photocatalysis of rhodamine B,” *Journal of Inorganic and Organometallic Polymers and Materials*, vol. 30, pp. 322–329, 2020.
- [32] A. Phuruangrat, P.-O. Keereesaensuk, K. Karthik et al., “Synthesis and characterization Ag nanoparticles supported on Bi₂WO₆ nanoplates for enhanced visible-light-driven photocatalytic degradation of rhodamine B,” *Journal of Inorganic and Organometallic Polymers and Materials*, vol. 30, pp. 1033–1040, 2020.
- [33] H. T. M. Thanh, N. T. T. Tu, N. P. Hung, T. N. Tuyen, T. X. Mau, and D. Q. Khieu, “Magnetic iron oxide modified MIL-101 composite as an efficient visible-light-driven photocatalyst for methylene blue degradation,” *Journal of Porous Materials*, vol. 26, pp. 1699–1712, 2019.
- [34] L. T. T. Tuyen, D. A. Quang, T. T. T. Toan et al., “Synthesis of CeO₂/TiO₂ nanotubes and heterogeneous photocatalytic degradation of methylene blue,” *Journal of Environmental Chemical Engineering*, vol. 6, no. 5, pp. 5999–6011, 2018.
- [35] J. S. Roy, G. Dugas, S. Morency, S. J. L. Ribeiro, and Y. Messaddeq, “Enhanced photocatalytic activity of silver vanadate nanobelts in concentrated sunlight delivered through optical fiber bundle coupled with solar concentrator,” *SN Applied Sciences*, vol. 2, Article ID 185, 2020.
- [36] R. Atchudan, T. N. J. I. Edison, S. Perumal, D. Karthikeyan, and Y. R. Lee, “Facile synthesis of zinc oxide nanoparticles decorated graphene oxide composite via simple solvothermal route and their photocatalytic activity on methylene blue degradation,” *Journal of Photochemistry and Photobiology B: Biology*, vol. 162, pp. 500–510, 2016.
- [37] N. T. V. Hoan, N. N. Minh, T. T. K. Nhi et al., “TiO₂/diazonium/graphene oxide composites: synthesis and visible-light-driven photocatalytic degradation of methylene blue,” *Journal of Nanomaterials*, vol. 2020, Article ID 4350125, 15 pages, 2020.
- [38] N. R. Khalid, A. Hammad, M. B. Tahir et al., “Enhanced photocatalytic activity of Al and Fe co-doped ZnO nanorods for methylene blue degradation,” *Ceramics International*, vol. 45, Part A, no. 17, pp. 21430–21435, 2019.
- [39] Z. Sun, C. Li, G. Yao, and S. Zheng, “In situ generated g-C₃N₄/TiO₂ hybrid over diatomite supports for enhanced photodegradation of dye pollutants,” *Materials & Design*, vol. 94, pp. 403–409, 2016.
- [40] J. R. Kim, B. Santiano, H. Kim, and E. Kan, “Heterogeneous oxidation of methylene blue with surface-modified iron-amended activated carbon,” *American Journal of Analytical Chemistry*, vol. 4, no. 7A, pp. 115–122, 2013.
- [41] N. T. T. Tu, P. C. Sy, T. T. Minh et al., “Synthesis of (Zn/Co)-based zeolite imidazole frameworks and their applications in visible light-driven photocatalytic degradation of Congo red,” *Journal of Inclusion Phenomena and Macrocyclic Chemistry*, vol. 95, pp. 99–110, 2019.
- [42] Y. Li, L. Li, C. Li, W. Chen, and M. Zeng, “Carbon nanotube/titania composites prepared by a micro-emulsion method exhibiting improved photocatalytic activity,” *Applied Catalysis A: General*, vol. 427–428, pp. 1–7, 2012.
- [43] Y. L. Hu, L. Q. Zhou, H. F. Liu, and X. P. Guo, “Visible light photocatalytic degradation of methylene blue over N-doped TiO₂,” *Key Engineering Materials*, vol. 609–610, pp. 141–146, 2014.
- [44] A. Houas, H. Lachheb, M. Ksibi, E. Elaloui, C. Guillard, and J.-M. Herrmann, “Photocatalytic degradation pathway of methylene blue in water,” *Applied Catalysis B: Environmental*, vol. 31, no. 2, pp. 145–157, 2001.
- [45] Y. Xu and M. A. A. Schoonen, “The absolute energy positions of conduction and valence bands of selected semiconducting minerals,” *American Mineralogist*, vol. 85, no. 3-4, pp. 543–556, 2000.
- [46] Y. Lin, H. Shi, Z. Jiang et al., “Enhanced optical absorption and photocatalytic H₂ production activity of g-C₃N₄/TiO₂ heterostructure by interfacial coupling: a DFT+ *U* study,” *International Journal of Hydrogen Energy*, vol. 42, no. 15, pp. 9903–9913, 2017.
- [47] J. Tian, Y. Sang, Z. Zhao et al., “Enhanced photocatalytic performances of CeO₂/TiO₂ nanobelt heterostructures,” *Small*, vol. 9, no. 22, pp. 3864–3872, 2013.
- [48] N. Suganthi, S. Thangavel, and K. Kannan, “*Hibiscus subdariffa* leaf extract mediated 2-D fern-like ZnO/TiO₂ hierarchical nanoleaf for photocatalytic degradation,” *FlatChem*, vol. 24, Article ID 100197, 2020.
- [49] H. Seema, K. C. Kemp, V. Chandra, and K. S. Kim, “Graphene-SnO₂ composites for highly efficient photocatalytic degradation of methylene blue under sunlight,” *Nanotechnology*, vol. 23, no. 35, Article ID 355705, 2012.